1991ApJ...366..203L

THE ASTROPHYSICAL JOURNAL, **366**:203–220, 1991 January 1

FAR-INFRARED AND SUBMILLIMETER-WAVELENGTH OBSERVATIONS OF STAR-FORMING DENSE CORES. I. SPECTRA

E. F. LADD,[1,2,3,4] FRED C. ADAMS,[1,4] S. CASEY,[3,4,5] J. A. DAVIDSON,[3,4,6] G. A. FULLER,[1,4]
D. A. HARPER,[3,4,5] P. C. MYERS,[1,2,3,4] AND R. PADMAN[4,7]

Received 1990 February 20; accepted 1990 June 27

ABSTRACT

We present far-infrared and submillimeter photometry of 10 low-mass star formation regions containing embedded *IRAS* sources. These new observations define the peak of the spectral energy distributions of these objects and provide more precise estimates of their bolometric luminosities. Two new sources, L1527 and L483, are among the reddest known low-mass objects, with spectral energy distribution peaks at 100–200 μm and extremely steep *IRAS* slopes. These cold sources have spectra which are similar to blackbodies of 30–40 K but have significant excess emission on the Wien side. Models of the spectral energy distributions using a spherically symmetric core structure indicate that these sources have visual extinctions greater than 1000 mag. However, models with these large extinctions predict too little near-infrared emission. We suggest that a non-spherically symmetric distribution of circumstellar material may play a role in the generation of the extra near-infrared emission.

Subject headings: infrared: sources — infrared: spectra — stars: circumstellar shells — stars: formation

I. INTRODUCTION

More than 100 visually opaque condensations in nearby dark clouds are known to be locations of relatively dense gas ($n \geq 10^4$ cm^{-3}) from observations of molecular spectral lines of ^{13}CO, C^{18}O, HC$_5$N, NH$_3$, and CS (Benson 1983; Myers, Linke, and Benson 1983; Myers and Benson 1983; Benson and Myers 1989; Zhou *et al.* 1989; and Fuller 1989). The *IRAS* satellite showed that about half of these "dense cores" are associated with *IRAS* point sources. About half of these sources are optically visible T Tauri stars, and half are optically invisible sources, with luminosities similar to that of T Tauri stars (Beichman *et al.* 1986; Myers *et al.* 1987). These optically invisible stars, deeply embedded in their parent cores, are thought to be the youngest known low mass stars, with ages of order a few times 10^5 yr. They are probably still in the process of acquiring their main sequence mass via infall from the surrounding core.

The spectral energy distribution, a plot of log νS_ν versus log ν, where ν is the frequency and S_ν is the flux density, is an important diagnostic of the stellar luminosity and of the structure of circumstellar temperature and optical depth. The spectral energy distribution provides an opportunity to examine the physical conditions within a dense core as a star is forming, before it becomes optically visible and can be placed on the Hertzsprung-Russell diagram.

The first observations of deeply embedded young massive stars showed that most of the luminosity from compact H II regions is radiated at far-infrared wavelengths near 100 μm rather than at optical and ultraviolet wavelengths, where an unextinguished OB star radiates most of its luminosity (Low and Aumann 1970; Harper and Low 1971). This displacement of the spectral peak indicates that circumstellar dust grains absorb optical and ultraviolet photons from the star and radiate in the far-infrared. More detailed spectral observations showed that the spectral energy distribution is usually much broader than expected from a single-temperature blackbody; this finding indicates that the circumstellar dust must have a wide range of temperature and thus must be distributed over a wide range of distances from the star (Scoville and Kwan 1976).

As the sensitivity of far-infrared observations improved, it was found that these properties of spectral energy distributions for relatively luminous, massive stars also hold for low-mass stars. Sources deeply embedded in dense cores such as B335 and L1551 have luminosities 1–30 $L_\odot$, similar to that of nearby, optically visible T Tauri stars; yet their spectral energy distributions peak near 100 μm. Most embedded sources resemble L1551 in their broad spectra, requiring a wide range of temperatures, but a well-known exception is the cold, narrow-spectrum source in B335 (Keene *et al.* 1983; Davidson 1987).

Adams, Lada, and Shu (1987, hereafter ALS) grouped low-luminosity spectral energy distributions into three classes corresponding to (1) optically invisible sources with spectral energy rising toward long wavelengths over 1–100 μm, and with spectral energy distributions broader than a blackbody; (2) visible T Tauri stars with spectral energy falling toward long wavelengths, and with spectral energy distributions broader than a blackbody; and (3) visible "post–T Tauri" stars with spectral energy falling toward long wavelengths, and with spectral energy distributions of a slightly reddened blackbody. They suggested that these groups trace an evolutionary progression in the development of a young star and accounted for this development with models of (1) a protostar, a circumstellar disk, and a rotating, collapsing dense core; (2) a T Tauri star with a disk and a "post-infall" core, or with only a disk; and (3) a post–T Tauri star with neither disk nor core. These

---

[1] Harvard-Smithsonian Center for Astrophysics.

[2] Visiting Astronomer at the NASA Kuiper Airborne Observatory.

[3] Visiting Astronomer at the NASA Infrared Telescope Facility, which is operated by the University of Hawaii under contract with the National Aeronautics and Space Administration.

[4] Visiting Astronomer at the James Clerk Maxwell Telescope, which is operated by the Royal Observatory Edinburgh on behalf of the Science and Engineering Research Council of the United Kingdom, the Netherlands Organization for Scientific Research, and the National Research Council of Canada.

[5] Yerkes Observatory, University of Chicago.

[6] NASA/Ames Research Center.

[7] University of Cambridge.

1991ApJ...366..203L

models are physically self-consistent and fit most of the data points of the typical spectral energy distributions within a factor of 3, over a range of some two decades in frequency and three decades in intensity.

To understand better the spectral properties and development of a forming star, it is necesssary to measure and explain all significant contributions to its luminosity, especially in the youngest objects. This task requires definition of the peak of the spectral energy distribution, usually with measurements in the wavelength range 100–300 μm. This range was not covered by *IRAS*, and because of severe atmospheric attenuation, it must be observed from airborne or satellite platforms. Thus relatively few of the optically invisible sources in dense cores have been observed with sufficient wavelength coverage to define their luminosities and spectral peaks accurately. Four are known with well-defined spectral peaks longward of 100 μm (L1551, L723, B361, and B335; Davidson 1987), and only one of these, L1551, was modeled by ALS.

This paper is the first report of a series of far-infrared and submillimeter wavelength observations, intended to define the luminosity and spectral shape of the emission from the youngest stars in nearby dark clouds. We present observations of 12 such sources, associated with dense cores (as defined by ammonia line emission; see Myers and Benson 1983 and Benson and Myers 1989). The *IRAS* emission from these sources is discussed by Beichman *et al.* (1986), and their near-infrared and optical emission is discussed by Myers *et al.* (1987). This paper presents and discusses spectral energy distributions; maps and spatial structure will be presented in future papers.

For the sake of clarity and consistency, we define the terms we will use to describe the sources in this paper. The region where gravitational infall energy is converted into radiative luminosity will be labeled the "stellar source." The stellar source typically is contained within a few hundred AU of the forming star and contains the star, any associated disk, or any other material generating luminosity from infall. The surrounding "core" contains the remainder of the gas and dust which is gravitationally bound to the stellar source. The core in systems forming low-mass stars typically extends to ~0.1 pc.

II. OBSERVATIONS

The new observations presented here are submillimeter and far-infrared bolometer measurements made using a variety of

TABLE 1A

OBSERVATIONS

Core Name	Right Ascension[a] (1950)	Declination[a] (1950)	Date Observed	Telescope[b]	Wavelength (μm)
L1489	$04^h01^m40^s.6$	26°10′49″	1987 Mar	KAO	100, 160
			1987 Oct	IRTF	350
			1989 Jan	JCMT	800
L1535	04 32 31.5	24 02 07	1987 Sep	KAO	100, 160
L1527	04 38 48	25 57 05	1987 Mar	KAO	100, 160
			1987 Oct	IRTF	350
			1989 Jan	JCMT	450, 800
L43	16 31 37.7	−15 40 52	1989 May	KAO	150, 190
L483	18 14 50.6	−04 40 49	1988 May	KAO	100, 160, 190
L673B	19 18 01.3	11 16 27	1988 May	KAO	100, 160, 190
L673A	19 18 04.6	11 14 12	1988 May	KAO	100, 160, 190
L1082A	20 52 04.7	60 03 18	1988 May	KAO	160
L1172A	21 01 44.2	67 42 24	1988 May	KAO	100, 160
L1031B	21 45 27.9	47 18 12	1988 May	KAO	100, 160
			1989 May	KAO	190
			1987 Oct	IRTF	350
			1989 Oct	JCMT	800

[a] The pointing centers for the maps are taken from Myers *et al.* 1987 where available, or the *IRAS Point Source Catalog.*

[b] KAO, NASA Kuiper Airborne Observatory, Moffett Field, CA; IRTF, NASA Infrared Telescope Facility, Mauna Kea, HI; JCMT, James Clerk Maxwell Telescope, Mauna Kea, HI.

TABLE 1B

INSTRUMENTAL PARAMETERS

Telescope	Backend	Filter (μm)	$\nu_{\rm eff}$[a] (GHz)	$\Delta\nu$[a] (GHz)	Field of View	Resolution	Sensitivity[b] (Jy)	Chopper Throw
KAO	Yerkes 32 element bolometer	100	3105	1348	300″	45″	4.	300″
		160	1670	522	300	50	5.	300
		190	1351	392	300	58	5.	300
IRTF	Yerkes 32 element bolometer	350	772	394	300	45	1.	300
JCMT	UKT-14 bolometer	450	685	84	120[c]	15	0.2	120[d]
		800	394	103	120[c]	15	0.1	120[d]

[a] Effective frequency and width are determined for a flat spectral source and no attenuating water vapor. The values for $\nu_{\rm eff}$ are the transmission-weighted mean frequencies, except for the JCMT values, which are the average of the two frequencies where the filter response is 50% of maximum.

[b] Typical 1 σ noise levels for the mapping data presented here.

[c] The JCMT field of view is determined by the size of the map made. These values are typical of our maps.

[d] The actual chopper throw was 60″ but the map was raster-scanned in the chopper direction and later reconstructed with NOD2 analysis software, creating an effective chop of 120″.

telescopes. The observation dates and telescopes used are listed in Table 1A. The typical instrumental parameters are summarized in Table 1B.

We observed several of these sources with the James Clerk Maxwell Telescope (JCMT) using the facility instrument UKT-14, a single-element germanium bolometer, in a chopped raster scanning mode. The chopper spacing was 60″ in azimuth for all observations, and the raster scans typically sampled 2 arcmin^2 on the sky. Broad-band filters centered on 450 and 800 μm were used during the observations. Calibration and atmospheric correction were obtained from frequent observations of Mars, the JCMT primary calibrator, as well as Jupiter and the point sources HL Tau and CRL 618. The Jovian fluxes from the observations of Griffin *et al.* (1986) were assumed. The fluxes for HL Tau and CRL 618 were determined from comparison with the planetary measurements and found to be consistent with the observations of Sandell (1989) and Adams, Emerson, and Fuller (1990).

The rest of the observations listed in Table 1A were acquired using the Yerkes Observatory Array Cameras, 32 element arrays of helium-cooled silicon bolometers, each mounted in an integrating cavity and illuminated through compound parabolic cones with a beam of approximately 45″ (see Hildebrand 1986; Harper *et al.* 1976). At wavelengths shorter than 200 μm, we observed with the NASA Kuiper Airborne Observatory (KAO); the 350 μm data were observed using the NASA Infrared Telescope Facility (IRTF). To cancel sky emission, a chopping secondary was employed, with chop rates of 9–30 Hz. The telescope was nodded approximately every 10 s during an integration such that the source spends equal time in the left and right chopper beams.

The filters used in the Yerkes Camera observations consist of combinations of capacitive and inductive metal-mesh transmission filters (Whitcomb and Keene 1980) with short-wavelength blocking provided both by a 1.6 mm polyethylene window coated with diamond dust and by quartz lenses in the field optics. The spectral characteristics of the filters used are displayed in Table 1B.

The 32 channels are arranged on a 6 × 6 square grid (without the corners), separated by approximately 48″, such that a single observation produces an undersampled map covering a 5′ × 5′ region on the sky. In order to obtain a fully sampled map, the array was moved through a sequence of eight pointings, each separated from the next by 12″ or 24″ offsets.

Calibration was accomplished by comparison of source fluxes to the fluxes of planets or other bright known calibrators. Attenuation by water vapor was tracked on the KAO by facility water vapor radiometers and at the IRTF by frequent observations of calibration sources. The calibration procedure involves assuming a spectral shape for both the calibrator and the program source, as well as an absolute flux for the calibrator (e.g., Loewenstein *et al.* 1977). In general, the source spectrum assumed is a cool (20–60 K) blackbody moderated by a dust emissivity law with a ν^β dependence where β varies between 1 and 2 (Hildebrand 1983). The calibrators were Mars, Jupiter, M82, and W51. The spectral shape of the atmospheric attenuation function is assumed to be constant in time. Its overall normalization is determined from the water vapor measurements. The uncertainty in the derived flux densities is estimated to be 30%–40%, due to the uncertainty in the calibrator fluxes and the atmospheric attenuation.

The flux densities listed in the accompanying plots represent the difference between the on-source flux and off-source fluxes determined from several off-source positions in each image. The sources presented here typically are composed of two spatial components—a pointlike central source just resolved by our observations, and a low-intensity plateau of emission extending 2′ or more from the pointlike source. Table 2 shows the flux densities measured by our observations of the peak single beam, and a 1 arcmin^2 box centered on the position of peak emission. In the spectra shown in this work, we will use the flux density contained within a 1 arcmin^2 box centred on the image peak rather than the peak single-beam flux density or the total integrated flux density. For objects located nearby, this method excludes some flux density from the core, resulting in an underestimate of the total emission, especially at long wavelengths. Therefore, when we compare the long-wavelength emission from nearby objects in § IV, we will include flux from a larger area. A discussion of the extent and nature of the resolved emission is reserved for future work.

III. RESULTS

We report on 12 candidate protostars, of the type discussed by Beichman *et al.* (1986), based on their proximity to known dense cores in molecular clouds, and on their infrared colors as delineated by *IRAS*. These sources have spectra rising with wavelength through the *IRAS* bands. Their 100 μm flux den-

TABLE 2

FAR-INFRARED AND SUBMILLIMETER FLUX DENSITIES

Core Name	Wavelength (μm)	Single-Beam Flux (Jy)	1′ Flux (Jy)	Map rms[a] (Jy)
L1489	100	55	74	5.3
	160	46	56	3.0
	350	4.8	8.4	0.8
	800	0.3	1.5	0.08
L1535	100	24	31	4.4
	160	38	45	4.6
L1527	100	47	89	4.3
	160	69	94	6.2
	350	12	22	1.1
	450	3.2	14	0.2
	800	0.5	1.4	0.08
L43	160	70	79	5.7
	190	38	38	4.7
L483[b]	100	130	170	6.7
	160	270	290	6.7
	190	160	140	7.8
L673B	100	19	19	2.9
	160	33	49	5.7
	190	44	36	7.8
L673A	100	11	15	2.9
	160	56	69	2.7
	190	53	54	5.4
L1082A	160	15	20	7.0
L1172A	100	10	11	2.2
	160	6	10	1.5
L1031B	100	67	80	5.1
	160	86	100	4.0
	190	110	120	5.0
	350	5.4	7.7	1.4
	800	0.3	1.5	0.02

[a] The map rms values give only the random component of the uncertainty in our maps. These values are *not* the errors in the measured fluxes listed above. The above measurements are also subject to systematic errors of 30%–40%.

[b] These values for L483 are subject to larger than normal systematic errors due to the lack of accurate water vapor information on two KAO flights. The errors in these fluxes are 40%–50%.

TABLE 3

CORE PROPERTIES

Source	Distance (pc)	Distance Reference	Outflow Reference	NH_3 Core Size (pc)	Core/Stellar Source Separation (D/R)[a]	NH_3 Reference
L1489	140	1	7	0.07	0.7	13
L1551	140	1	8	0.12	0.1	14
L1535	140	1	9	0.09	0.5	15
L1527	140	1	9	0.08	0.0	13
L43	160	2	7	0.13	0.7	13
L483	200	...	10	0.18	0.0	16
L673B	300	3	11	0.34	0.9	16
L673A	300	3	11	0.34	0.2	16
B335	250	4	12	0.11	0.4	13
L1082A	440	5	7	0.59	0.4	13
L1172A	440	5	7	0.19	0.5	13
L1031B	900	6	7	0.86	0.3	13

[a] The projected distance between the peak of the observed NH_3 emission and the stellar sources is measured in units of the FWHM of the NH_3 core map.

REFERENCES.—(1) Elias 1978*c*; (2) Elias 1978*a*; (3) Herbig and Jones 1983; (4) Tomita, Saito, and Ohtani 1979; (5) Viotti 1969; (6) Elias 1978*b*; (7) Myers *et al.* 1988; (8) Snell and Schloerb 1985; (9) Heyer *et al.* 1987; (10) Parker *et al.* 1988; (11) Armstrong and Winnewisser 1988. The large-scale outflow observed is coincident with both L673A and L673B; (12) Frerking and Langer 1982; (13) Benson and Myers 1989; (14) Torrelles *et al.* 1983; (15) Ungerechts, Walmsley, and Winnewisser 1982; (16) Benson 1989.

sities are greater than ~10 Jy, making them likely candidates for detectable far infrared emission. Table 3 summarizes the general properties of the sources discussed in this work. All but two of these objects show evidence of mass outflow. Six are located (in projection) within the half-maximum contour of their associated dense cores as measured by the $NH_3(J, K) = (1, 1)$ emission. With two exceptions (L1082A and L1031B), the cores observed are similar in size (~0.1 pc) and mass (~10 $M_\odot$; Benson and Myers 1989). As a group, these 12 sources represent many of the different manifestations of low mass star formation.

The spectral energy distributions for these 12 protostellar sources are displayed in Figure 1. These spectra include the observations discussed above as well as measurements from the *IRAS Point Source Catalog* and other previously published observations. The spectra of the well-known infrared sources L1551 (IRAS 04287+1801) and B335 (IRAS 19345+0727) contain no new data and are presented for comparison only.

All of the sources emit most of their luminosity in the infrared, and most of them peak at about 100 μm. The spectra can be divided into three groups: (*a*) those with a single maximum near 100 μm and little near-infrared emission (B335, L1527, L483, L673A, L673B), (*b*) those with a single maximum near 100 μm and a significant wing of near infrared emission (L1535, L1551, L1082A, L1172A), and (*c*) those with two maxima or one broad maximum where the near-infrared luminosity rivals the contribution from the far-infrared (L43, L1489, L1031B). These groups are similar to classes 1 and 2 of ALS, based on the slope of the infrared spectral energy distribution. Further comparison with the ALS classes is discussed in § IV.

a) Comparison with Published Results

The new submillimeter and far-infrared results appear to fit well with previously published observations. In most cases, the 160 μm and 200 μm measurements smoothly extrapolate the curve traced by the *IRAS* data. At 100 μm, the KAO flux densities agree with the *IRAS Point Source Catalog* measurements within the error bars in all but one case (L1172D). However, in all cases, the KAO points are systematically higher than the *IRAS* values, typically by 20%. This unexplained systematic deviation has been noted previously in *IRAS Explanatory Supplement* (1988) when comparing IRAS flux densities of Uranus with the KAO measurements of Hildebrand *et al.* (1985). We adopt the KAO 100 μm measurements in this work to be consistent with our other far-infrared data.

b) Total Luminosities

We present luminosities derived from the observations presented here, *IRAS* measurements, and other previously published data. Since all of the sources peak in the spectral regime sampled by the KAO measurements, the systematic uncertainty in these measurements dominates the uncertainty in the calculated luminosity. In some cases, however, the lack of complete spectral coverage adds an additional uncertainty. The luminosities are listed in Table 4.

Nine of the 12 νF_ν distributions in Figure 1 have peaks well defined by the far-infrared and submillimeter observations reported in this paper. On the near-infrared side, the shortest wavelength measurement or upper limit presented here has a spectral energy density typically less than 10% (and often less than 1%) of the peak spectral energy density. On the far-infrared side, however, the coverage is not as good. In four cases (L483, L1172A, L673A, and L673B) there is only one measurement on the long-wavelength side of the spectral energy density peak, and in two cases (L1082A and L1535), the peak of the spectral energy distribution may not be reached at our longest wavelength measurement.

In an attempt to correct for the incomplete long-wavelength coverage, we have linearly extrapolated the longest wavelength measurement to zero flux density at zero frequency and calculated the resulting luminosity. This correction generally increases the luminosity by less than 5% in the five sources for which we have data at wavelengths longer than 200 μm. Four sources have corrections in excess of 20%—L1535, L673A, L1082A, and L1172A. These sources do not have the peak of their spectral energy distributions well defined by our observations. Hence, luminosity estimates for these objects remain somewhat uncertain. If the spectral energy distributions peak at a wavelength less than 190 μm, as do all of the other sources whose peaks are defined, then our data indicate that this cor-

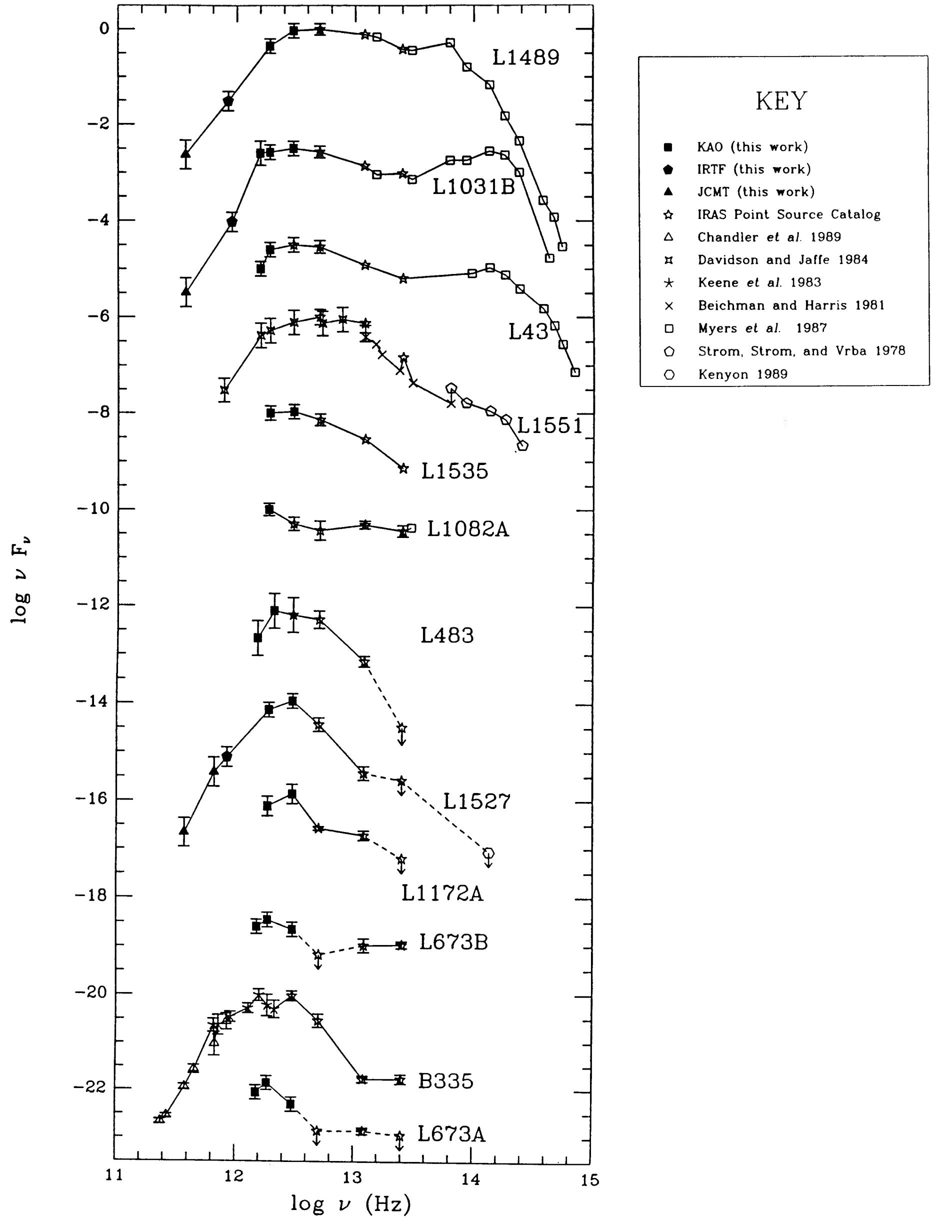

FIG. 1.—Spectral energy distributions for the 12 sources presented in this work. The filled points denote new observations presented here for the first time. The data values for these sources can be found in Table 3 and the referenced works.

TABLE 4

DERIVED SPECTRAL PROPERTIES

Source	Peak νF_ν (10^{-12} W m^{-2})	Frequency of Peak νF_ν (THz)	Luminosity ($L_\odot$)	Fraction of Luminosity Emitted at $\lambda > 60$ μm	Mean Frequency[a] (THz)	Inner Slope[a]
L1489	2.4	5.0	4.4	0.3	17.	−0.5
L1551	19	5.0	24	0.5	7.4	−1.6
L1535	0.9	3.0	1.2	0.6	4.2	−0.9
L1527	2.7	3.0	2.1	0.8	4.3	−2.4
L43	1.9	3.0	3.5	0.5	28.	−0.7
L483	6.2	2.1	14	0.6	3.9	−0.9
L673B	2.6	1.9	6.0	0.7	4.0	−1.6
L673A	0.9	1.9	5.8	0.8	3.3	−1.4
B335	1.3	1.6	4.0	0.8	2.7	−1.4
L1082A	0.4	1.9	4.5	0.6	6.4	−0.6
L1172A	0.3	3.0	2.6	0.8	3.7	−1.4
L1031B	2.4	3.0	223	0.4	49.	−0.6

[a] As defined in § III*c*.

1991ApJ...366..203L

rection overestimates the additional luminosity due to unobserved long-wavelength flux.

On the high-frequency side of the spectral energy distribution we have truncated the luminosity calculation at the highest frequency measurement. Where upper limits occur at the high-frequency end of the spectrum, we have treated the first limit as a measured data point. It is difficult to estimate the contribution to the luminosity from the unmeasured near-infrared and optical part of the spectral energy distribution. However, sources for which we have near-infrared and optical data (e.g., L1489, L1551, and L1031B) suggest that the slope of F_ν is at least as steep as $\nu^{-2.6}$. For the sources which have no measurements shortward of 12 μm, we have extrapolated F_ν from 12 μm with a $\nu^{-2.6}$ power law and find that the additional luminosity due to this extrapolation is never greater than 0.1 $L_\odot$.

In addition to these errors introduced by the lack of complete spectral coverage, the uncertainty in the flux density measurements themselves must also be considered. We estimate the errors in the calculated luminosities are 30% for the sources with observations at wavelengths longer than 200 μm and up to 50% for the other sources.

The luminosities we derive are presented in Table 4. On average, they exceed those calculated from only the *IRAS Point Source Catalog* data by a factor of 2. The increased luminosity comes from emission between 100 and 200 μm which was undetectable by *IRAS*. Longward of 200 μm, the flux density from these sources drops off considerably, and the additional luminosity is negligible.

More than half of the spectral energy is emitted at wavelengths longer than 60 μm for eight of the 12 sources presented here. For these sources, *IRAS* estimates are clearly lower limits to the emitted luminosity. Table 2 contains the new luminosities as well as the fraction of the luminosity which is emitted at wavelengths longer than 60 μm. This fraction seems to correlate well with the morphological descriptions of the spectra given above. In general, the "wide" and double-humped spectra have a very small fraction of their energy emitted at wavelengths longer than 60 μm, while the essentially blackbody-like spectra have a significant fraction of their energy emitted at these long wavelengths.

c) *Spectral Shapes*

The spectral shapes in our sample vary from the double-peaked shape of L1031B to the relatively narrow single-peaked spectrum of L1527. The other sources have intermediate shapes which form a smooth progression between the two extremes (see Fig. 1). In all cases, these sources have more far-infrared flux density and less near-infrared and optical flux density than do T Tauri stars such as DG Tau and T Tau.

The spectra in Figure 1 are arranged from top to bottom in order of increasing percentage of total flux emitted at wavelengths longer than 60 μm (see also Table 4). The main difference between the upper and lower sources in this figure is the excess near-infrared component in the broad spectrum sources. The far-infrared and submillimeter shapes, where well defined, show little variation, while the near-infrared shapes vary more from source to source. We interpret the differences in spectral shapes in §§ IV and V.

The long-wavelength measurements presented here define the spectral energy distribution peaks and extend the range of spectral shapes beyond those previously known. Figure 2*a* shows the normalized spectra of L1489, L1527, and L1031B plotted for comparison with data for the two T Tauri stars DO Tau (see Adams, Emerson, and Fuller 1990, and references therein) and SU Aur (see ALS, and references therein). The long-wavelength data ($\lambda \geq 60$ μm) for L1527 are well fitted by a $T = 30$ K blackbody moderated by an emissivity law of the form given in Hildebrand (1983), while SU Aur resembles a stellar blackbody of 4000 K. In each case, however, there is a significant excess—on the high frequency (Wien) side of the peak for L1527, and on the low frequency (Rayleigh-Jeans) side of the peak for SU Aur, as illustrated in Figure 2*b*. The low frequency excess in T Tauri stars and other moderately extinguished ($A_V \sim 10$) objects has been discussed by ALS and others, as has the high-frequency "excess" in ALS class 1 protostars such as L1551 and L1489 ($A_V \lesssim 100$). However, the spectra of L1527, B335, and L483 presented here make clear that even the coldest, most extinguished sources have high-frequency excesses over a blackbody. This excess makes little contribution to the total luminosity, but it is important for understanding the source structure and radiative transfer, as discussed in § V.

The other spectra in Figure 2*a* have shapes between the extremes of L1527 and SU Aur. L1551 peaks at 100 μm as does L1527, but it has a greater excess on the high-frequency side, reaching into the optical. L1031B has far-infrared and near-infrared peaks of similar height. DO Tau and L1551 have "mirror image" spectra. DO Tau has a hot blackbody spectrum with an excess on the low-frequency side.

Figure 2 is representative of much of the data in this paper (see also ALS and Myers *et al.* 1987), in that there appear to be only two spectral regions where νF_ν distributions have maxima: either ~ 100 μm or ~ 1 μm. None of the sources from ALS, Myers *et al.* (1987), or this work, has a $\nu F \nu$ peak near 10 μm. None of the five sources with data at wavelengths longer than 200 μm has a maximum beyond 200 μm. Two sources, L1031B and VSSG 23 (see ALS), have double peaks, one occurring at ~ 100 μm and the other at ~ 1 μm.

Since these spectral energy distributions are complex and difficult to classify, we will quantify them by taking the first moment of their flux density distributions. This quantity, which we will call the mean frequency, $\bar{\nu}$, gives some measure of the "redness" of a given observed spectral energy distribution. The quantity $\bar{\nu}$ is defined by

$$\bar{\nu} = \frac{\int_0^{\nu_{\max}} \nu F_\nu \, d\nu}{\int_0^{\nu_{\max}} F_\nu \, d\nu} ,$$

where the integrals are piecewise linear from zero frequency to $\nu_{\max}$, the highest frequency point detected. In contrast to the frequency of the peak of the spectral energy distribution, which has a bimodal distribution, $\bar{\nu}$ varies smoothly from 3×10^{12} Hz (100 μm) to 3×10^{14} Hz (1 μm) in this sample. T Tauri stars generally have higher mean frequencies than the more embedded objects, though their large infrared excesses reduce the mean frequency below the peak of their νF_ν distributions. Likewise, the embedded sources tend to have mean frequencies greater than the peak of their νF_ν distributions because they have excesses on the high-frequency side of their spectral energy distributions.

The accuracy of the mean frequency calculation depends weakly on the spectral coverage. In all cases, the contribution from a linear extrapolation of F_ν from our longest wavelength point to zero frequency reduces the mean frequency $\bar{\nu}$ by less than 1%. The contribution from the high-frequency side can be

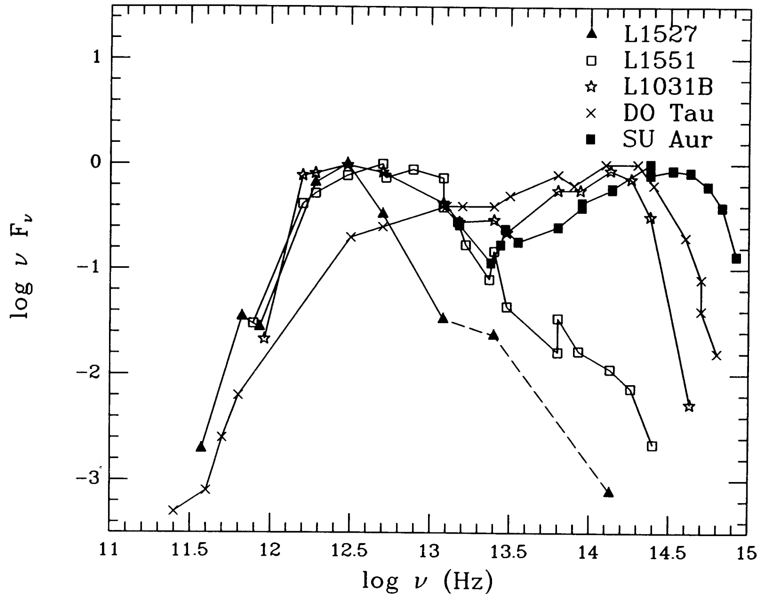

FIG. 2*a*

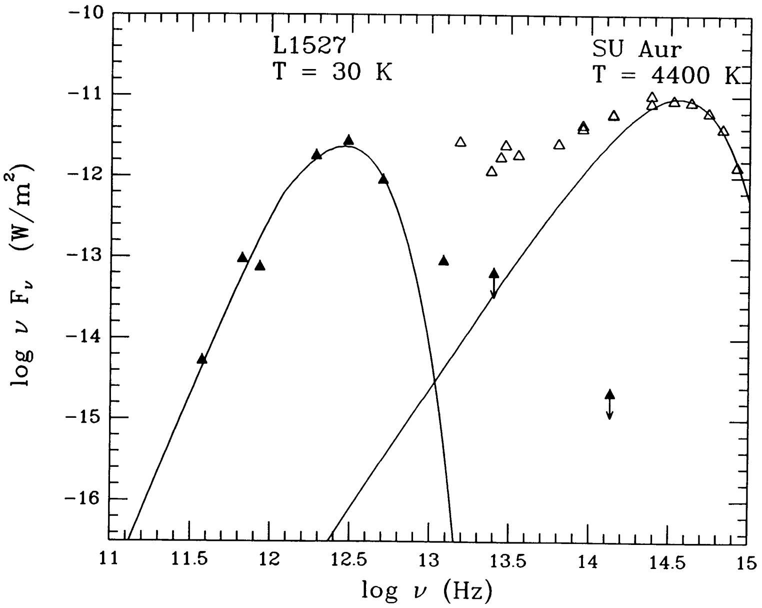

FIG. 2*b*

FIG. 2.—Normalized spectral energy distributions of selected sources in our sample and selected T Tauri stars from Adams, Emerson, and Fuller (1989). The sources in (*a*) show that the spectral energy distribution peaks in either the far-infrared or the near-infrared, but not in between. Furthermore, the shapes of the spectral energy distributions range from the cool blackbody-like spectrum of L1527, to the wide, double-humped shape of L1031B, to the hot blackbody spectrum of SU Aur. In (*b*) L1527 and SU Aur are plotted with best-fit blackbodies. Note that in both cases, there is an excess of emission in the frequency regime $5 \times 10^{12} < \nu < 5 \times 10^{13}$. The blackbody fit for L1527 has been multiplied by an emissivity law of the form described in Hildebrand (1983).

estimated by again using a $\nu^{-2.6}$ power law to extrapolate F_ν from the highest frequency measurement. This correction never increases the mean frequency $\bar{\nu}$ by more than 20%.

The mean frequency correlates with measures of the slope of the spectral energy distribution. In Figure 3*a*, we have plotted the mean frequency versus the inner slope,[8] a measure of the slope of the spectral energy distribution near its peak. The correlation between mean frequency and spectral slope extends over two decades in mean frequency, indicating that objects with different mean frequencies also have different spectral shapes. The correlation in Figure 3*a* between $\bar{\nu}$ and slope is easily understood as a property of curves which can only peak at one of two values, and it shows that the mean frequency is a good estimator of the mid-infrared slope.

---

[8] The inner slope s is defined by

$$s = \frac{\log (\nu_0 F_{\nu 0}/\nu_1 F_{\nu 1})}{\log (\nu_0/\nu_1)}$$

where the spectral energy distribution has its maximum value $\nu_0 F_{\nu_0}$ at frequency ν_0, and where $\nu_1 = 4\nu_0$ if $\nu_0 < \bar{\nu}$ as is the case for the 12 sources presented in this work, or $\nu_1 = \nu_0/4$ if $\nu_0 > \bar{\nu}$ as is the case for T Tauri stars. The correlation in Fig. 3*a* holds for many different measures of the spectral slope.

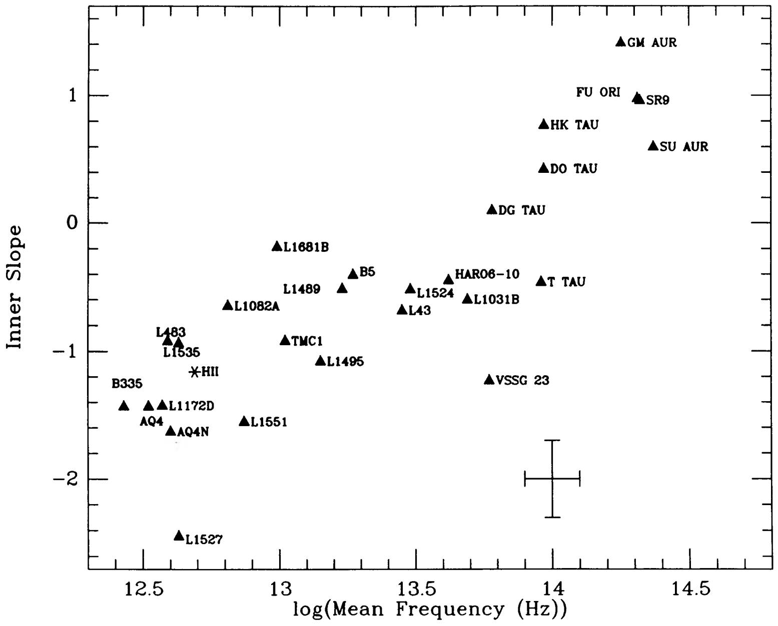

FIG. 3*a*

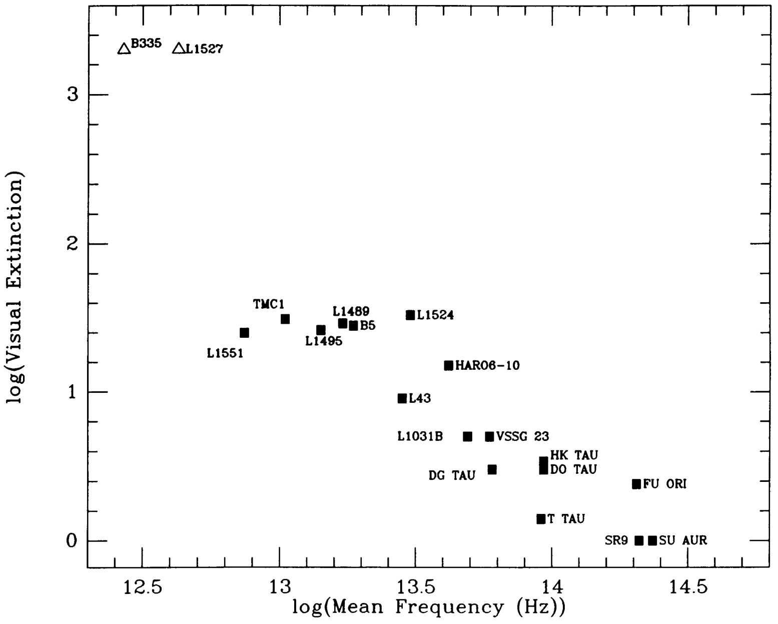

FIG. 3*b*

FIG. 3.—(*a*) The correlation between the spectral mean frequency and the inner slope (as defined in § IIIc). In addition to the sources discussed in this paper, this figure also contains data from Myers *et al.* (1987) and some of the sources discussed by ALS, Adams, Lada, and Shu (1988), and Adams, Emerson, and Fuller (1990). The starred point in this figure shows the location of the compact H II regions discussed by Chini, Krügel, and Wargau (1987). The error bar shown in the lower right-hand corner is indicative of the estimated uncertainties in the two quantities plotted. (*b*) The correlation between mean frequency and the visual extinction to the stellar source. Except for B335 and L1527 (*open triangles*), the visual extinctions are from Myers *et al.* (1987), ALS, Adams, Lada, and Shu (1988), and references contained therein, and all are observationally based values. For B335 and L1527 the extinctions are derived from models presented in this work. As discussed in the text, for all the sources except the most lightly extinguished, the observational extinction should probably be regarded as a lower limit to the true line of sight extinction to the stellar source.

ALS, Myers *et al.* (1987), and others have suggested that the spectral slope is a measure of evolutionary development. However, this slope is sometimes difficult or impossible to measure because it depends strongly on choice of wavelength, or because the spectral shape is too complex to have a well-defined slope. The mean frequency of a spectral energy distribution can always be well determined as long as the peak of the spectrum is sampled. Furthermore, it uses all of the available data for a given source and not just the data from one narrow wavelength region.

The mean frequency also correlates very well with published estimates of the extinction to the objects as might be expected, since the extinction plays a major role in determining the spectral shape (Fig. 3*b*; see also Adams 1989). However, no correlation exists between mean frequency and source luminosity. This result is clearly evident from the point on Figure 3*a* which shows the typical slope and mean frequency of compact H II regions (Chini, Krugel, and Wargau 1987). The luminosity of these objects is of order 10^3–10^6 times larger than that of most of the objects in Figure 3*a*, yet this high-luminosity point does not stand out from the low-luminosity objects. Among the wider spectra, L1031B has over an order of magnitude greater luminosity than that of T Tauri stars, but it is located on Figure 3*a* with a collection of low-luminosity objects. This insensitivity to luminosity suggests that extinction is more important than total luminosity in determining the spectral shapes of these objects.

IV. COMPARISON OF OBSERVATIONS AND THEORY

Models describing protostellar emission involving a hot source of luminosity centered within a centrally condensed envelope of gas and dust have shown that the emergent spectral energy distribution is both broader and cooler than the spectrum of the central source (see, e.g., Larson 1969 and Scoville and Kwan 1976). These models show that for a radial power-law density distribution, the resulting radial temperature dependence is also nearly a power law. They also indicate that high-frequency radiation ($\lambda < 10\ \mu$m) is generated in the inner parts of the core ($r \lesssim 1000$ AU) and that long-wavelength emission is generated in the outer parts of the core which typically contain the bulk of the core mass. In this section, we compare four of the observed spectral energy distributions in Figure 1 with two models of emission from star/core systems. We first describe the theoretical models and then examine the fits to the sources.

a) The Adams-Shu Model

In the model of protostellar emission developed by Adams and Shu (1985, 1986; hereafter the AS model), the protostellar system consists of three principal components: the forming star itself, a circumstellar disk, and an infalling envelope of gas and dust. Each component produces a contribution to the total radiation field.

The forming star is assumed to form from a slowly rotating isothermal cloud core. The initial conditions for star/core emission are determined by the sound speed a and rotation rate Ω of the core. For a given set of initial conditions, the collapse calculation can be performed (see Shu 1977 and Terebey, Shu, and Cassen 1984, hereafter TSC) to determine the density distribution of the infalling envelope. The collapse naturally produces a core/envelope structure, with a central hydrostatic object (i.e., the forming star) surrounded by an infalling envelope of dust and gas.

This collapse progresses from "inside out" as an expansion wave propagates outward at the sound speed. The head of the wave defines the boundary of the collapse region at $r_H = at$, where t is the time since the beginning of the collapse. Outside this radius, the cloud is static; inside this radius, the flow quickly approaches free-fall velocities. The flow remains nearly spherical outside a centrifugal radius, $R_C = G^3M^3\Omega^2/16a^8$, the position at which the infalling material with the highest specific angular momentum will encounter a centrifugal barrier (see TSC). Inside the radius R_C, the flow becomes highly nonspherical. In the region immediately surrounding the star, the temperature will be too high for dust grains to exist and an opacity-free zone will result (see Stahler, Shu, and Taam 1980).

The luminosity of the AS models is generated by both a star and disk. As discussed in AS (see also ALS), the total luminosity depends in part on the efficiency η_D with which material is accreted in the disk and the efficiency η_* with which rotation energy is dissipated in the star. In this present work, we vary these efficiencies to produce the observed bolometric luminosities of the sources.

The AS model adopts the quasi-static approximation: the physical structure of the object at a particular instant in time (in particular, the density distribution) is determined by the collapse scenario outlined above. The radiative transfer calculation is then performed using this quasi-static structure. Interstellar dust grains (a mixture of graphite and silicate) provide the dominant contribution to the opacity (see Draine and Lee 1984). We have added a 3.1 μm ice feature to the opacity law for consistency with ALS and Adams and Shu (1986). This extra feature has no effect on the large-scale shape of the derived spectral energy distributions. At far-infrared wavelengths, the scattering cross section of these grains is much smaller than the absorption cross section; hence, the effects of scattering are neglected in this treatment. In the near-infrared, the effects of scattering are not negligible; we will discuss these effects in § V.

This model uses the technique of an "equivalent spherical envelope" by taking the spherical average of the nonspherical density distribution produced by the rotating infall solution (see AS, TSC). This approach includes the main effects of rotation—a less centrally concentrated infalling envelope which leads to a lower column density, a lower luminosity for a given infall rate due to the storage of energy in the form of rotation, and the production of a circumstellar disk—while retaining a spherical radiative transfer calculation.

b) The Wolfire-Cassinelli Model

The model of protostellar emission developed by Wolfire and Cassinelli (1986, 1987; hereafter the WC model) is qualitatively similar to the AS model described above. In the WC model, the protostellar system consists of two components: the forming star and a spherical envelope of dust and gas extending to a radius of 0.1 pc.

The properties of the surrounding dust envelope can be specified to be any power law in radial distance r from the star, with an inner radius defined by the temperature at which each constituent grain will melt, and an outer radius specified by the user. Up to 18 different grain types and sizes can be included in the model. As in the AS model, the temperature and emitted radiation are calculated for each individual grain type. Similarly, the properties of the central source—the total luminosity L and, the stellar source temperature T_{star}—can also be specified independent of any dynamical model.

In using the WC model, we require that the luminosity of the model fit our observations and constrain the outer radius to be 0.1 pc. We fix the chemical abundances to be solar (10% He and 89% H) and the model fixes the dust grain size distribution to be the MRN mixture (Mathis, Rumpl, and Nordsieck 1977). For each source, we choose an input stellar source temperature based on the near infrared observations of Myers *et al.* (1987) and others. The remaining free parameters, total column density, and density power-law index α, are varied to provide acceptable fits.

The main difference between the two models is that the WC model adopts a parametric approach, whereas the AS model adopts a self-consistent approach. The WC model has the advantage that it can consider a much wider range of possible configurations; the AS model has the advantage that it is based on a consistent physical picture of protostellar theory. Both models have been run with similar input parameters and produce similar results. Taken together, these two models provide a useful theoretical context with which to compare the observed spectra, as we discuss below. The model parameters used in the following fits are summarized in Tables 5A and 5B.

The output spectral energy distribution from both models contains all of the emission generated by the stellar source and processed by the core. The core in both the WC and AS models extends to a radius of approximately 0.1 pc from the stellar source. For objects in Taurus, the model cores are larger than the 1 arcmin^2 region we have integrated to determine the observed flux densities. At a distance of 140 pc, the AS model predicts that a 1 arcmin^2 box will detect only 33% of the total long-wavelength ($\lambda \gtrsim 300\ \mu$) flux density generated, since much of the long-wavelength flux is emitted from the outer core. Therefore, to compare our 350 μm fluxes from objects in Taurus with these models, we have calculated the total flux generated within a $3' \times 3'$ (0.12 pc) box centered on the peak emission pixel. The JCMT maps ($\lambda = 450$ and 800 μm) extend only over a 1 arcmin^2 region and cannot be augmented.

For both models, "best fits" are determined somewhat subjectively. Fits are considered acceptable if they have the same luminosity as the source and if the peak of the spectral energy distribution matches the observations. In general more attention was paid to the data near the peak of the spectral energy distribution, rather than the high-frequency data where scattering effects might play a role, or the very low frequency data, which may be biased by the beam size chosen.

c) The Narrow Sources

i) *L1527*

The spectral energy distribution of L1527 is among the narrowest presented in this work and contains very little near-infrared emission. The observed spectral energy distribution is shown in Figure 4*a* along with theoretical spectra from both the AS and WC models. The AS fit to the spectrum uses $M = 0.1\ M_\odot$, $a = 0.35$ km s^{-1}, and $\Omega = 10^{-13}$ rad s^{-1}. These parameters produce a total system luminosity of $L_{\rm bol} = 3.8\ L_\odot$ and a total extinction to the central source $A_V \sim 1900$ mag.

The WC models shown are similar to the AS model, for $r > R_C$, in that the density decreases with radius as an $r^{-1.5}$ power law. The two WC models (labeled WC1 and WC2 in Fig. 4*a*) have a total luminosity of 2.45 $L_\odot$ generated by a 3600 K blackbody of radius 2.8×10^{11} cm. The outer radius of the core is set at 0.1 pc.

The WC1 fit is similar to the AS fit in the near-infrared and has a total extinction of 3900 mag. The higher extinction WC2 model ($A_V = 5800$ mag) does not overestimate the 60 μm data, as do the WC1 model and the AS fit, but it severely underestimates the 25 μm flux density.

The most interesting aspect of the models of this object is the very large visual extinction required to replicate the spectral energy distribution. Physically, this large extinction is necessary to prevent mid-infrared radiation ($\lambda \sim 10\ \mu$m) from escaping from the system and contributing to the observed infrared fluxes.

TABLE 5A

WC MODEL PROPERTIES

		INPUT PARAMETERS			OUTPUT PARAMETERS	
MODEL	$T_{\rm star}$ (K)	Luminosity ($L_\odot$)	Density[a] (10^{-19} g cm^{-3})	α	Luminosity ($L_\odot$)	A_V (mag)
WC1	3600	2.4	8	1.5	2.44	3900
WC2	3600	2.4	16	1.5	2.43	11000
WC3	3600	2.4	1	1.6	2.57	1400
WC4	3600	2.4	0.5	1.8	2.42	6400
WC5	3600	2.4	4	1.5	2.46	2000
WC6	3600	2.4	12	1.3	2.36	830
WC7	2500	4.0	12	1.5	4.12	5900
WC8	2500	4.0	60	1.2	3.92	1700
WC9	2500	4.0	30	1.3	4.03	2000
WC10	5000	15	5	1.5	15.2	1400
WC11	5000	15	30	1.0	14.7	180
WC12	5000	5.0	2	1.5	5.01	740

[a] The mass density is specified at a distance of 0.1 pc from the center of the model.

TABLE 5B

AS MODEL PROPERTIES

		INPUT PARAMETERS				OUTPUT PARAMETERS	
MODEL	$M_{\rm star}$ ($M_\odot$)	Ω (10^{-14} rad s^{-1})	a (km s^{-1})	η_d	η_s	Luminosity ($L_\odot$)	A_V (mag)
AS1	0.1	10	0.35	0.25	0.50	3.05	1900
AS2	0.1	10	0.35	0.00	0.50	2.19	2000
AS3	1.0	10	0.35	0.50	1.00	26.6	86
AS4	0.1	2	0.20	1.00	0.50	6.72	53

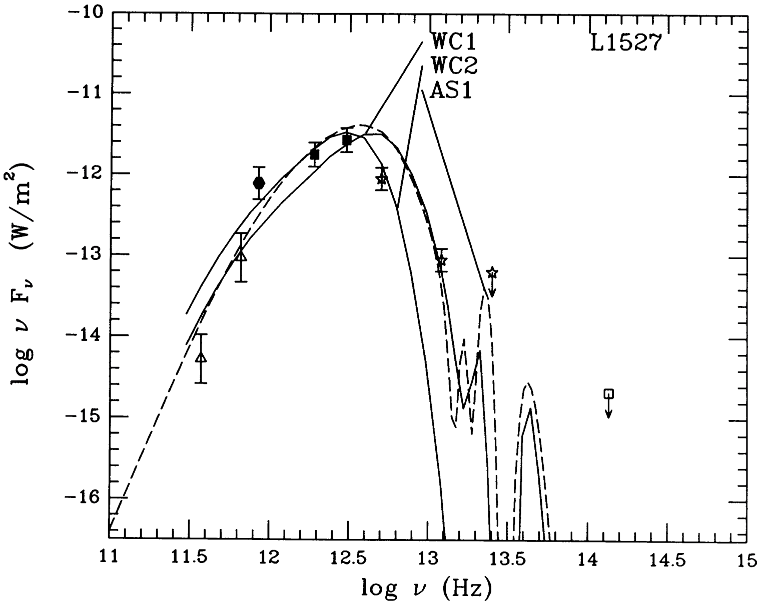

FIG. 4*a*

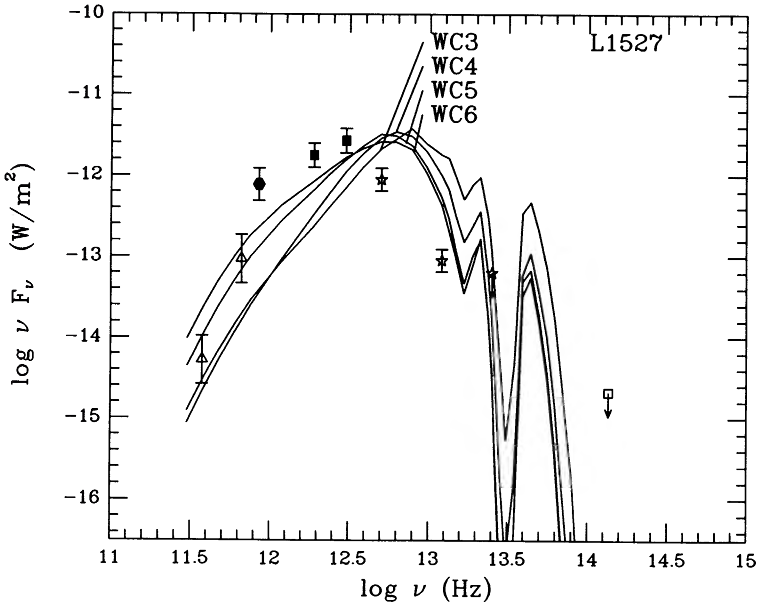

FIG. 4*b*

FIG. 4.—AS and WC fits to the spectral energy distribution of L1527. The input parameters and derived quantities for each fit are summarized in Tables 5A and 5B. All of the long-wavelength data values are given in Table 2, except for the 350 μm data point which includes flux from a 3′ × 3′ box centered on the peak emission pixel.

WC models with less extinction can be created either by reducing the overall scale factor on the dust density distribution or by reducing α. We have created several lower extinction WC models to test whether a high extinction is really required to fit L1527. By varying α, we can create many spectral shapes, but in all cases, the lower extinction fits contain too much near-infrared emission to be acceptable. Figure 4*b* shows the lowest extinction models for four different values of α—1.3, 1.5, 1.6, and 1.8. In each of these cases, the models overshoot the 25 μm and 60 μm measurements, and several exceed the 12 μm upper limit. The extinctions in these models range from 830 mag ($\alpha = 1.3$) to 6400 mag ($\alpha = 1.8$). We conclude that the extinction to the stellar source in L1527 must be greater than 800 mag.

ii) *B335*

B335 has a spectral energy distribution similar to L1527 in that it is narrow and has very little near-infrared component. However, it differs from L1527 in that it peaks at a longer wavelength (190 μm; L1527 peaks at 100 μm). The observed spectral energy distribution for this source is shown in Figure 5*a* along with the theoretical spectra from the AS and WC models. The AS fit to the spectrum uses $M = 0.1\ M_{\odot}$, $a = 0.35$ km s^{-1}, and $\Omega = 10^{-13}$ rad s^{-1}, The derived visual extinction

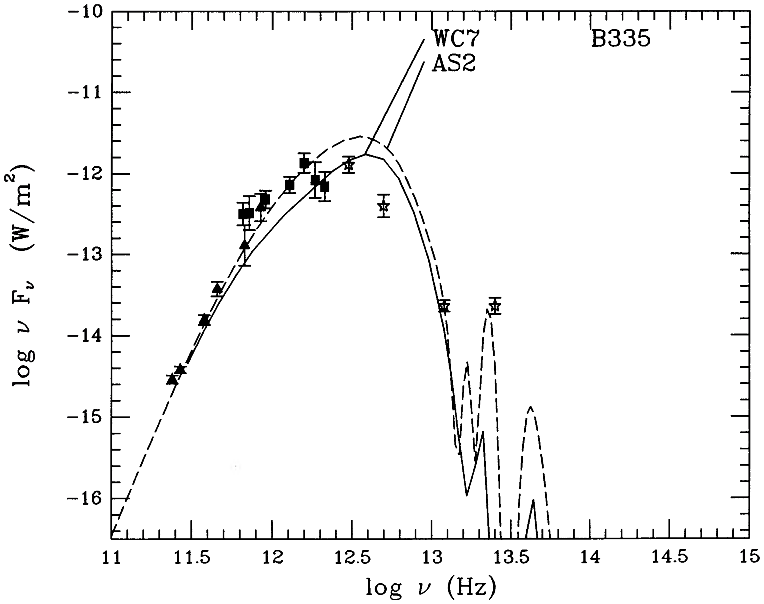

FIG. 5*a*

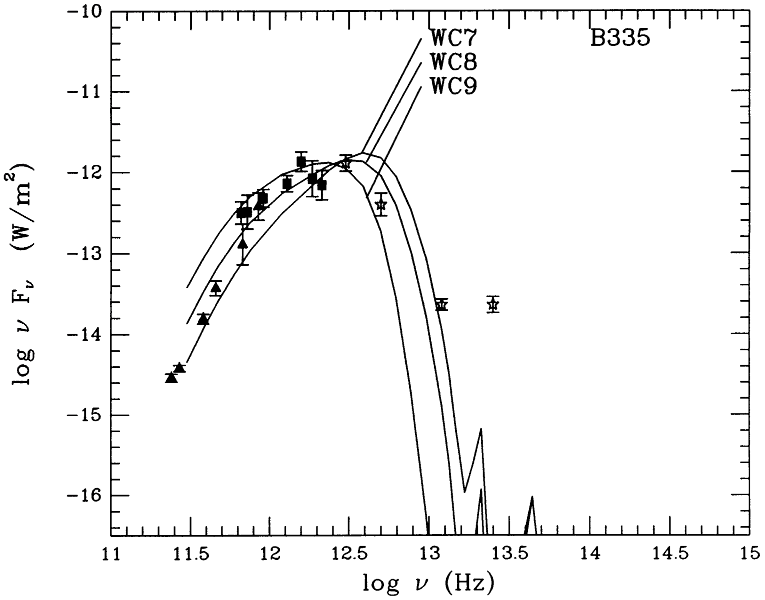

FIG. 5*b*

FIG. 5.—AS and WC fits to the spectral energy distribution of B335. The input parameters and derived quantities for each fit are summarized in Tables 5A and 5B.

to the stellar source is 2000 mag and the total luminosity generated is 2.2 $L_\odot$. The WC fit with $\alpha = 1.5$ has a total luminosity of 4.1 $L_\odot$ and a visual extinction of 5900 mag.

The quality of the WC fits to the far-infrared and submillimeter portions of the spectral energy distribution can be affected by changes in α. As α is reduced, more of the core's mass and opacity is located in the outer parts of the core and is therefore cooler. As a result, the spectral energy distribution peaks at longer wavelengths, and far-infrared and submillimeter flux densities are enhanced. Figure 5*b* shows that changes in the density power-law index α can materially affect the submillimeter fit. We find that the best submillimeter fit for B335 has $\alpha = 1.2$ and a total visual extinction of 1700 mag.

The analysis presented so far has ignored the near-infrared side of the spectral energy distribution. Although the coldest and narrowest spectra presented here (e.g. L1527, B335, and L483) can be well-fitted by blackbody spectra at the peak and on the long-wavelength side of their spectral energy distributions, there is a slight excess of near-infrared emission over the predicted blackbody flux. A power-law fit to νF_ν versus ν for a 40 K blackbody curve between 60 μm and 25 μm gives a power-law index of 5.8, while the steepest values from our data are 4.2 (B335) and 3.6 (L1527).

The more sophisticated AS and WC models also have trouble fitting the near-infrared side of B335 and L1527. In both models, high extinction is required to push the peak of the spectral energy distribution to longer wavelengths and to reduce the $\sim$50 μm flux density below observed upper limits.

However, because of the need for this high extinction, the model spectral energy distributions mimic a blackbody, and at wavelengths 10–100 μm the slope is again too steep to match the observed data. Neither the simple blackbody model nor the high extinction AS and WC models can completely explain the observed near-infrared slope on these narrow spectrum sources.

d) The Wide Sources

i) *L1551*

Sources with significant near-infrared excesses require models with lower visual extinction and are more complicated because the circumstellar environment and its structure have a direct impact on the emitted spectral energy distribution. L1551 is associated with infrared and optical nebulosity (e.g., Campbell *et al.* 1988). If the 1–5 μm emission is interpreted as purely attenuated starlight, the derived visual extinction is 17–26 mag. However, Campbell *et al.* (1988) and Moneti *et al.* (1988) note from their high spatial resolution images that the optical and infrared emission is *not* pointlike, but rather extended and "cometary" in shape. They interpret the near-infrared and optical emission as scattered light and suggest that $A_V \sim 20$ mag is only a lower limit to the true extinction to the star. Far-infrared measurements of the surrounding dense core indicate that the beam-averaged A_V is greater than 100 mag (Davidson and Jaffe 1984).

The spectral energy distribution of L1551 was modeled previously by ALS using the AS model. Here we show the observed spectral energy distribution in Figure 6*a* along with the theoretical spectra from both the AS and WC models. The AS fit to the spectrum uses $M = 1.0\ M_\odot$, $a = 0.35$ km s^{-1}, and $\Omega = 10^{-13}$ rad s^{-1} and yields a visual extinction of 86 mag and a luminosity of 27 $L_\odot$.

The WC models cannot easily fit a spectrum as broad as L1551 because they are so centrally condensed. A broad spectrum requires contriubtions to the total luminosity from dust at a broad range of temperatures and thus at a broad range of distances from the stellar source. However, to provide adequate flux densities in the far-infrared requires significant densities in the cold outer core. This excess material, combined with the power-law increase in density with decreasing radius, provides too much extinction to let the near-infrared emission escape. Conversely, if the extinction is lowered to allow circumstellar near-infrared emission to escape, too little material remains in the outer core to provide significant far-infrared flux. Hence broad spectra, with significant contributions to the total luminosity from 1 to 100 μm, are difficult to replicate in the WC model.

We have tried to fit the mid- and far-infrared portions of the spectral energy distribution and have neglected the excess emission at wavelengths less than 5 μm. The two WC fits shown in Figure 6*a* have a luminosity of 15 $L_\odot$. WC 10 has a visual extinction to the stellar source of 1400 mag and $\alpha = 1.5$, while WC 11 has an extinction of 176 mag and $\alpha = 1.0$. Because of the lower values of α, WC 11 is a broader spectrum, but it still is not as wide as the observed data.

Both WC spectral energy distributions have very deep silicate absorption features at 10 μm, which are not seen in the data. The cold outer core material which is responsible for suppressing the near infrared flux also generates this deep feature. Because rotation in the AS model reduces the dust density at $r < R_C$, the AS model has a lower total column density, and it matches the observed 10 μm silicate dip more closely than the WC model.

An alternate fit to the spectral energy distribution using the AS model is shown (see the dashed curve in Fig. 6*b*) using an opacity law of the form $\kappa_\nu \propto \nu^{3/2}$ at low frequencies (long wavelengths, i.e., $\lambda > 60$ μm). The "standard" opacity law advocated by Draine and Lee (1984; see also Draine 1989) and adopted by both AS and WC has the form $\kappa_\nu \propto \nu^2$ at low frequencies. However the submillimeter frequency dependence of the opacity law could be less steep (perhaps due to icy mantles on dust grains). Since the two opacity laws are constrained to produce the silicate spectral features in the 10–30 μm wavelength range, the $\kappa_\nu \propto \nu^{3/2}$ law has a larger opacity at submillimeter wavelengths and the corresponding spectral energy distribution is more luminous (in the submillimeter regime) than that obtained using the $\kappa_\nu \propto \nu^2$ opacity law (see Fig. 6*b*). This boost is submillimeter emission from the same density distribution broadens the model spectral energy distribution and produces a slightly better fit.

ii) *L1489*

The spectral energy distribution of L1489 has an even greater near infrared "excess" than L1551. The visual extinction, determined from the near infrared observations of Myers *et al.* (1987), is 29 mag, but the imaging polarimetry of Heyer *et al.* (1990) has shown that much of the near-infrared emission is scattered. Heyer *et al.* (1990) conclude that the extinction determined from near-infrared observations is a lower limit to the true visual extinction to the stellar source.

The observed spectral energy distribution is shown in Figure 7 along with theoretical spectra from both the AS and WC models. This source was modeled previously by ALS using the AS model with $M = 0.1\ M_\odot$, $a = 0.20$ km s^{-1}, and $\Omega = 2 \times 10^{-14}$ rad s^{-1}. As with L1551, the best WC fits to the mid- and far-infrared severely underestimate the near-infrared flux. The best WC model with $\alpha = 1.5$ has a total visual extinction of 745 mag and a total luminosity of 5 $L_\odot$.

While the mid-infrared spectrum of L1489 can be fitted by both models, the near- and far-infrared parts of the spectrum are more difficult. As with L1551, the near-infrared flux from L1489 is largely scattered emission for $\lambda \leq 3$ μm. Both the AS and WC models underestimate the emission in this region, but when the maximum correction for scattering calculated by ALS is applied (see the Appendix of ALS), the theoretical model can produce more emission than is observed. Therefore, we argue that models with a proper treatment of the scattered emission can accurately reproduce the near infrared spectrum of L1489.

e) Summary

In the preceding subsections, we have shown that very high visual extinctions ($A_V \gtrsim 1000$ mag) are sometimes required to fit the far-infrared and submillimeter portions of the observed spectral energy distributions as well as to reduce the near-infrared component below observed limits. In the narrowest spectra (L1527 and B335), the high-extinction models account for most of the observed luminosity. However, even in these cases, the model spectra cannot account for the slope of the spectral energy distribution at wavelengths between 12 μm and 60 μm.

In the wider spectra (L1489 and L1551), we find that high-extinction models fit the far-infrared part of the spectrum but underestimate the near-infrared flux. Models which reduce the

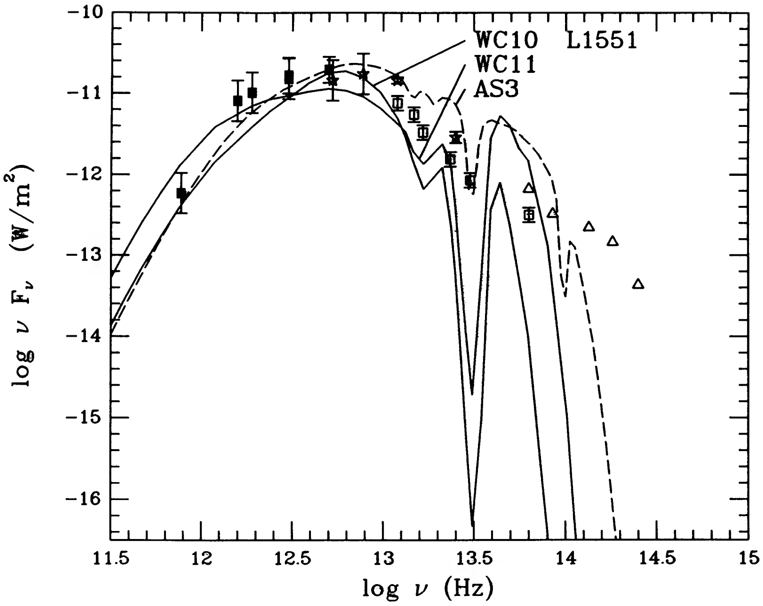

FIG. 6*a*

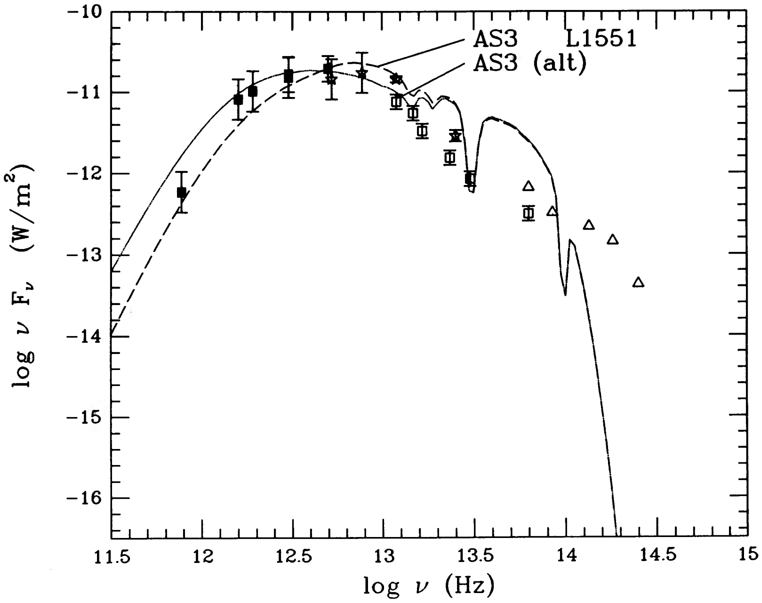

FIG. 6*b*

FIG. 6.—AS and WC fits to the spectral energy distribution of L1551. The input parameters and derived quantities for each fit are summarized in Tables 5A and 5B. In (*b*) the AS fit from (*a*) is plotted along with the fit using the alternate opacity discussed in the text.

circumstellar density without severely affecting the outer core density, by invoking (*a*) rotation (AS) or (*b*) a flatter power law density distribution (WC), can help reduce the visual extinction to the stellar source and provide some of the extra near-infrared emission required, without sacrificing much of the far-infrared flux. However, even these models cannot completely explain the far- and near-infrared components of the observed spectral energy distribution simultaneously. Like the narrow sources discussed above, these sources require an additional component of the radiation field, such as scattered light or nonspherical core geometry, to fully explain the detailed structure of the observed spectral energy distributions.

V. DISCUSSION

a) *Luminosity and Spectral Shape*

The additional wavelength coverage provided by the new data presented in this paper has allowed improved estimates for the luminosity of these sources. In most cases, the new data define the location of the peak of the spectral energy distribution, which typically lies between 100 and 160 μm. The data therefore constrain the long-wavelength contribution to the luminosity. The new luminosities, which have been derived using all the available data, do not exceed previous estimates

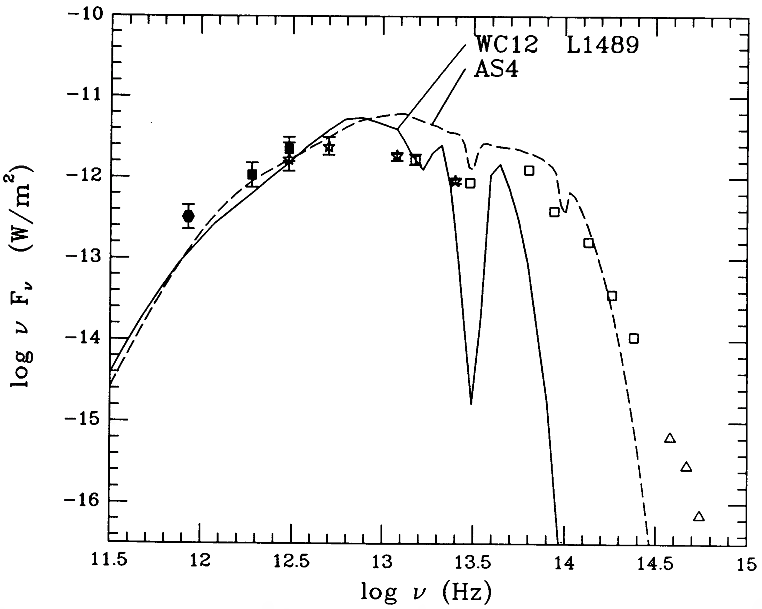

FIG. 7.—AS and WC fits to the spectral energy distribution of L1489. The input parameters and derived quantities for each fit are summarized in Tables 5A and 5B. All of the long-wavelength data values are given in Table 2, except for the 350 μm data point which includes flux from a 3′ × 3′ box centered on the peak emission pixel.

by more than a factor of 2–3, even for the reddest objects which we believe to be among the youngest known low-mass stars.

At wavelengths longer than 60 μm, little variation occurs in the shape of the spectra of the various sources. Most of the material in the cores is optically thin at these wavelengths, and since these observations were mostly made with beams covering more than 0.01 pc, the observed emission is dominated by the core. The degree of similarity in the long-wavelength emission of these objects probably reflects the similarity in the conditions in the outer core region; this claim is also suggested by observations of molecular lines in these regions (Benson and Myers 1989).

In contrast to their similarity at long wavelengths, the spectra show considerable variation at shorter wavelengths. For example L1031B emits 40% of its luminosity at wavelengths greater than 60 μm and an almost equal amount at wavelengths less than 10 μm, L1551 emits nearly 50% of its luminosity at wavelengths longer than 60 μm and a nearly negligible fraction (2%) shortward of 10 μm, and B335 emits 80% of its luminosity longward of 60 μm. The spectral characteristics of these objects exhibit a more or less smooth variation, as can be seen from Figures 1 and 3. As the near-infrared component of the spectral energy distribution increases, the mid-infrared slope of the spectrum decreases. According to the three class spectral classification scheme discussed by ALS, the objects in this paper fall into class 1, (objects with spectra which rise going from 1 to 100 μm), and class 2, (objects with approximately flat spectra).

ALS suggest that the three spectral classes of objects trace an evolutionary progression. The oldest objects are those with class 3 spectra which are visible T Tauri stars with optically thin or no circumstellar disks. The next youngest are the class 2 objects, T Tauri stars with disks and in some cases circumstellar envelopes. Class 1 objects represent the earliest stage of evolution and were identified by ALS as protostellar sources, those objects deriving significant luminosity from gravitational infall. L1551 has been discussed as representative of this group of objects. Compared to the older classes 2 and 3, these objects emit much less of their energy at mid- and near-infrared wavelengths. In this work we have identified two new objects, L1527 and L483, which are among the most extreme class 1 sources. These sources, like B335 and L723, emit an even smaller percentage of their luminosity in the near-infrared than does L1551.

b) *Sources with Narrow Spectra*

These objects (L1527, L483, and B335) are some of the coldest objects observed. They have long-wavelength spectra ($\lambda > 60$ μm) which closely resemble that of a single-temperature blackbody with temperatures in the range 30–40 K (e.g., Fig. 2*b*). Both the AS and WC models indicate that these objects have extremely high extinctions to the central source. Almost all the observed emission is reprocessed radiation from the core, rather than attenuated emission from the stellar source. The AS and WC multitemperature models of these sources tend to confirm the single-temperature models in that dust with the temperature 30–40 K is the dominant contributor to the observed luminosity. This emission originates primarily at a distance of ~300 AU from the center of the star/core system.

The AS and WC models of these cold cores fit most of the spectral energy distribution reasonably well. The *very* high extinctions ($A_V \sim 1000$ mag) in these models completely attenuate direct emission from the stellar source and force virtually all of the emitted photons to be reprocessed in the core. The resulting emitted flux, therefore, more directly samples the thermal conditions in the core, independent of the details of the stellar source which originally generates the luminosity. As a result, these model spectra are similar to the cool blackbodies used by Davidson (1987), Chandler *et al.* (1990), and others to fit the bulk of the observed spectrum.

While the foregoing AS, WC, and single temperature models fit the far-infrared parts of L1527, L483, B335, and similar sources, they can not completely account for the observed spectral slopes at both ~80 and ~30 μm (see Figs. 2*b*, 4a, 4*b*, and § IV). The 100 and 60 μm points fit best on a high-extinction, near-blackbody curve, but the 25 and 12 μm points lie significantly above a blackbody curve and the near-infrared slope is much flatter than a cold blackbody. A lower extinction model better approximates the 25 μm flux density but overestimates the 60 μm flux density by at least an order of magnitude and moves the peak of the spectral energy distribution shortward of 100 μm. Therefore, compared to the models which fit the bulk of the luminosity of the object, these objects have near infrared excesses.

c) *Sources with Broad Spectra*

Sources like L1551 and L1489 may have similar excesses on the near-infrared side of their spectra, although the evidence is not as clear. The differences between the models and the data are better described by differences in spectral slope than by excess near infrared emission. In all of the models presented above for L1551 and L1489, the near-infrared spectral shape tends to have more curvature than the observed data. As a result, the models typically tend to overestimate the emission at $\lambda \sim 20$ μm and underestimate the emission at $\lambda \sim 1$ μm.

By including the effects of scattering, we can create models which have flatter near-infared spectra and therefore fit the data better. However, scattering effects are usually negligible for wavelengths longer than ~5 μm and have little effect for $\lambda = 2$–5 μm (e.g., ALS; Draine and Lee 1984). Therefore, while scattered light probably cannot account for the excess emission seen in the narrow sources, it likely plays a role in the wider sources. The details of the scattering correction to the AS model have been discussed previously by ALS. A full treatment of scattering remains to be done but is beyond the scope of this present work.

d) *Circumstellar Structure*

i) *The Near-Infrared Excess*

In all of these sources, more radiation from warm dust close to the stellar source escapes to the observer than is predicted by AS and WC models. This effect might occur if the extinction around the stellar source is not as uniform as these spherically symmetric models assume. For example, there may be lines of sight to the stellar source which have lower than typical extinctions and thus allow a small fraction of the high frequency photons to escape to the observer.

ii) *Anisotropy in the Circumstellar Dust Density Distribution*

Estimates of the amount of material toward these objects using measurements at different wavelengths also suggest that the material is not uniformly distributed. For example, the NIR colors of L43 measured by Myers *et al.* (1987) indicate a visual extinction of 9 mag, whereas Levreault (1987) derives a value of 0.3 mag from the optical classification of the visible star. Similarly, Campbell *et al.* (1988) derive a visual extinction of between 17 and 26 mag for L1551 IRS 5 by assuming that the observed 1–5 μm emission is attenuated starlight, but FIR measurements indicate a beam-averaged A_V in excess of 100 mag (Davidson and Jaffe 1984). In each case, the estimate of A_V based on longer wavelength data exceeds the estimate based on shorter wavelength data. Evidently, the high-frequency emission is finding a low extinction path through these cores.

Recent NIR and optical images of some of these regions, e.g., L1551 (Campbell *et al.* 1988), L43 (Mathieu *et al.* 1988; Heyer *et al.* 1990), and L1489 (Heyer *et al.* 1990), show one-sided fan-shaped reflection nebulae which clearly indicate that much of the observed emission is not directly attenuated starlight but rather light scattered through cavities in the circumstellar core. In addition, theses studies indicate that the distribution of material very close to the stellar source is anisotropic.

Other observations clearly indicate of anisotropic material in the vicinity of these objects. Maps of the CO outflows associated with many of these objects (e.g., Myers *et al.* 1988; Terebey, Vogel, and Myers 1989) show that the outflows depart from spherical symmetry. In several objects, including L1551 and B335, the outflows are bipolar. Closer to the stellar souces, optical and infrared observations reveal complex emission structures, such as HH objects, jets, and regions of cometary nebulosity. In many of these objects, the regions of detected CO outflow are closely associated with the optical and near infrared nebulosity (see, e.g., Heyer *et al.* 1990; Reipurth and Bally 1986).

Nonspherical structure in the inner part of the core can arise for many possible reasons. Rotation of the original core as it collapsed can make the isodensity contours oblate as would the collapse of a magnetized core along the magnetic field lines (see, e.g., Lizano and Shu 1989). Even if the core remained perfectly spherical as it collapsed to form the star, an anisotropic wind from the star could sweep up gas and dust in a nonspherical manner. The material in the cores might not be smoothly distributed but somewhat clumpy. In addition, the stellar souce might be displaced from the center of symmetry in the core due to small relative motion. If we adopt an age of 10^4 yr for a source and assume that if the stellar source has a random component of velocity equal to one-quarter of the gas sound speed at 10 K ($=0.2$ km s^{-1}), then in 10^4 yr a stellar source can move 100 AU. This movement may introduce an asymmetry in the dust column density around the star.

Nonspherical structure, especially in the near-circumstellar environment, will provide photons from the stellar source with ray paths of differing extinction. Unlike the spherically symmetric case, where all stellar source flux encounters the same overlying extinction, an anisotropically distributed core can allow some flux to suffer significantly less than the average extinction for the core. This energy can provide the observed near-infrared excess in the narrow sources and can contribute to the flattening of the near infrared slope in the wider sources.

Lefevre, Daniel, and Bergeat (1983) and Dent (1988) have shown that significant amounts of near-infrared radiation can escape through the poles of an oblate distribution of circumstellar material. Preliminary modeling using an ad hoc core model with high and low column density paths has shown that core anisotropy can modify the derived spectral energy distributions to provid excess near-infrared flux. More rigorous modeling efforts are underway.

While the spectral energy distributions presented here do not prove the existence of anisotropically distributed circumstellar or core material, their detailed structure is not sufficiently explained by the standard spherically symmetric models. The AS and WC models fit the spectral energy distribution reasonably well over three decades in frequency, and so we conclude that the basic physics and initial conditions contained in these models are correct. However, the data depart from these models, especially on the near-infrared side of each spectral energy distribution, in a systematic fashion. This detailed structure can lead to refinements of the standard models. The possible modifications presented above—scattering and anisotropy in the surrounding core material—

are supported by other observational data. However, other considerations, such as changes in the dust grain properties or the opacity law (including the presence of tiny dust grains of polycyclic aromatic hydrocarbons) may also provide the desired refinements to the model spectral energy distributions.

VI. CONCLUSIONS

1. We present far-infrared and submillimeter photometry of 12 dense cores with embedded *IRAS* sources. These sources have spectral energy distribution peaks in the range 100–200 μm, too red to be determined by *IRAS* data alone. The luminosity is generally 3–30 $L_{\odot}$, characteristic of low-mass star/core systems. These luminosity estimates are generally twice as great as, and significantly more accurate than, those provided by *IRAS* data alone.

2. Two new sources, in L1527 and L483, are among the reddest known, with peak emission at 100–200 μm, and with extremely steep spectral slopes. Like B335, however, each has significant excess emission over the best-fit blackbody on the short-wavelength side of the peak: there, the emission is better described by a power law than by a declining exponential.

3. The spectra of the reddest sources are approximately blackbodies at 30 K, plus a short-wavelength excess, while the spectra of optically visible T Tauri stars are approximately blackbodies at 4000 K, plus a long-wavelength excess. The present data give further support to the idea that very young stars reduce their circumstellar extinction as they evolve, so that their infrared spectra become hotter and bluer with time.

4. The progression in spectral energy distribution from the reddest sources to the T Tauri stars is conveniently shown by a plot of two diagnostic parameters: the inner slope s versus the mean frequency of emission $\bar{\nu}$, evaluated over F_{ν}. For the sources presented here and for other young low-luminosity stars, s and $\bar{\nu}$ are highly correlated, suggesting a progression from heavily extinguished stars in cores, with $s \simeq -1.5$ and $\log \bar{\nu} \simeq 12.8$, to lightly extinguished T Tauri stars outside cores, with $s \simeq 0.5$ and $\log \bar{\nu} \simeq 14.0$.

5. The reddest stars must have visual extinction greater than 1000 mag, according to two independent radiative transfer models: (1) a rotating, collapsing dense core, with embedded protostar and circumstellar disk (Adams and Shu 1986), and (2) a star with no disk, but with a spherically symmetric circumstellar shell, having radial density power-law exponent as a free parameter (Wolfire and Cassinelli 1987). Both of these models fit the observed spectral energy distributions reasonably well.

6. To fit the typical far-infrared emission peak of the spectral energy distribution, many lines of sight through a source must have visual extinction of hundreds of magnitudes, or more. However, fitting the near-infrared emission requires that *some* photon paths have much lower column density, so that enough near-infrared photons which originate near the star can reach the telescope. A more complex source geometry involving the nonspherical distribution of circumstellar material can provide low column density photon paths. Such a geometry is suggested independently by evidence of outflow cavities, rotation, jets, and other circumstellar features which depart from spherical symmetry.

The authors gratefully acknowledge the assistance of R. Pernic, R. Lowenstein, G. Engargiola, and D. Cole of Yerkes Observatory in the KAO and IRTF data acquisition and the assistance of J. P. Emerson in the JCMT data acquisition. We also thank the staff of the KAO, IRTF, and JCMT for their assistance during our observing runs. This work was supported in part by NASA grant NAG-374.

REFERENCES

Adams, F. C. 1989, in *Infrared Spectroscopy in Astronomy—The 22nd ESLAB Symposium*, ed. B. H. Kaldeich (Noordwijk: ESA Publications), p. 233.
Adams, F. C., Emerson, J. P., and Fuller, G. A. 1990, *Ap. J.*, **357**, 606.
Adams, F. C., Lada, C. J., and Shu, F. H. 1987, *Ap. J.*, **312**, 788 (ALS).
Adams, F. C., and Shu, F. H. 1985, *Ap. J.*, **296**, 655.
———. 1986, *Ap. J.*, **308**, 836.
Armstrong, J. T., and Winnewisser, G. 1988, *Astr. Ap.*, **210**, 373.
Beichman, C. A., Myers, P. C., Emerson, J. P., Harris, S., Mathieu, R., Benson, P. J., and Jennings, R. E. 1986, *Ap. J.*, **307**, 337.
Benson, P. J. 1983, Ph.D. thesis, Massachusetts Institute of Technology.
———. 1989, private communication.
Benson, P. J., and Myers, P. C. 1989, *Ap. J. Suppl.*, **71**, 89.
Campbell, B., Persson, S. E., Strom, S. E., and Grasdalen, G. L. 1988, *A.J.*, **95**, 1173.
Chandler, C. J., Gear, W. K., Sandell, G., Hayashi, S., Duncan, W. D., Griffin, M. J., and Hazell, A. S. 1990, *M.N.R.A.S.*, in press.
Chini, R., Krugel, E., and Wargau, W. 1987, *Astr. Ap.*, **181**, 378.
Davidson, J. A. 1987, *Ap. J.*, **315**, 602.
Davidson, J., and Jaffe, D. 1984, *Ap. J.* (*Letters*), **277**, L13.
Dent, W. R. F. 1988, *Ap. J.*, **325**, 252.
Draine, B. T. 1989, in *Infrared Spectroscopy in Astronomy—The 22nd ESLAB Symposium*, ed. B. H. Kaldeich (Noordwijk: ESA Publications), p. 93.
Draine, B. T., and Lee, H. M. 1984, *Ap. J.*, **285**, 89.
Elias, J. H. 1978*a*, *Ap. J.*, **224**, 453.
———. 1978*b*, *Ap. J.*, **223**, 859.
———. 1978*c*, *Ap. J.*, **224**, 857.
Frerking, M. A., and Langer, W. D. 1982, *Ap. J.*, **256**, 523.
Fuller, G. A. 1989, Ph.D. thesis, University of California, Berkeley.
Griffin, M. J., Ade, P. A. R., Orton, G. S., Robson, E. I., Gear, W. K., Nolt, I. G., and Radostitz, J. V. 1986, *Icarus*, **65**, 244.
Harper, D. A., Hildebrand, R. H., Steining, R., and Winston, R. 1976, *Appl. Optics*, **15**, 53.
Harper, D. A., and Low, F. J. 1971, *Ap. J.* (*Letters*), **165**, L9.
Herbig, G. H., and Jones, B. F. 1983, *A.J.*, **88**, 1040.
Heyer, M. H., Ladd, E. F., Myers, P. C., and Campbell, B. G. 1990, *A.J.*, **99**, 1585.
Heyer, M. H., Snell, R. L., Goldsmith, P. F., and Myers, P. C. 1987, *Ap. J.*, **321**, 370.
Hildebrand, R. H. 1983, *Quart. J.R.A.S.*, **24**, 267.
Hildebrand, R. H. 1986, *Opt. Eng.*, **25**, 323.
Hildebrand, R. H., Lowenstein, R. F., Harper, D. A., Orton, G. S., Keene, J., and Whitcomb, S. E. 1985, *Icarus*, **64**, 64.
IRAS Catalogs and Atlases Explanatory Supplement. 1988, ed. C. A. Beichman, G. Neugebauer, H. J. Habing, P. E. Clegg, and T. J. Chester (Washington: GPO).
Keene, J., Davidson, J. A., Harper, D. A., Hildebrand, R. H., Jaffe, D. T., Loewenstein, R. F., Low, F. J., and Pernic, R. 1983, *Ap. J.* (*Letters*), **274**, L43.
Larson, R. B. 1969, *M.N.R.A.S.*, **145**, 271.
Lefevre, J., Daniel, J.-Y., and Bergeat, J. 1983, *Astr. Ap.*, **121**, 51.
Levreault, R. M. 1988, *Ap. J.*, **330**, 897.
Lizano, S., and Shu, F. H. 1989, *Ap. J.*, **342**, 834.
Loewenstein, R. F., *et al.* 1977, *Icarus*, **31**, 315.
Low, F. J., and Aumann, H. H. 1970, *Ap. J.* (*Letters*), **162**, L79.
Mathieu, R. D., Benson, P. J., Fuller, G. A., Myers, P. C., and Schild, R. E. 1988, *Ap. J.*, **330**, 385.
Mathis, J. S., Rumpl, W., and Nordsieck, K. H. 1977, *Ap. J.*, **217**, 425.
Moneti, A., Forrest, W. J., Pipher, J. L., and Woodward, C. E. 1988, *Ap. J.*, **327**, 870.
Myers, P. C., and Benson, P. J. 1983, *Ap. J.*, **266**, 309.
Myers, P. C., Fuller, G. A., Mathieu, R. D., Beichman, C. A., Benson, P. J., Schild, R. E., and Emerson, J. P. 1987, *Ap. J.*, **319**, 340.
Myers, P. C., Heyer, M., Snell, R. L., and Goldsmith, P. F. 1988, *Ap. J.*, **324**, 907.
Myers, P. C., Linke, R. A., and Benson, P. J. 1983, *Ap. J.*, **264**, 517.
Parker, N. D., Padman, R., Scott, P. F., and Hills, R. E. 1988, *M.N.R.A.S.*, **234**, 67P.
Reipurth, B., and Bally, J. 1986, *Nature*, **320**, 336.
Sandell, G. 1989, JCMT internal memo.
Scoville, N. Z., and Kwan, J. 1976, *Ap. J.*, **206**, 718.
Shu, F. H. 1977, *Ap. J.*, **214**, 488.
Snell, R. L., and Schloerb, F. P. 1985, *Ap. J.*, **295**, 490.
Stahler, S. W., Shu, F. H., and Taam, R. E. 1980, *Ap. J.*, **241**, 637.
Terebey, S., Shu, F. H., and Cassen, P. 1984, *Ap. J.*, **286**, 529 (TSC).
Terebey, S., Vogel, S. N., and Myers, P. C. 1989, *Ap. J.*, **340**, 472.
Tomita, Y., Saito, T., and Ohtani, H. 1979, *Pub Astr. Soc. Japan*, **31**, 407.

Torrelles, J., Rodríguez, L. F., Cantó, J., Carral, P., Marcaide, J., Moran, J. M., and Ho, P. T. P. 1983, *Ap. J.*, **274**, 214.
Ungerechts, H., Walmsley, C. M., and Winnewisser, G. 1982, *Astr. Ap.*, **111**, 339.
Voitti, N. R. 1969, *Mem. Soc. Astr. Italiana*, N.S., **40**, 75.
Whitcomb, S. E., and Keene, J. 1980, *Appl. Optics*, **19**, 197.
Wolfire, M. G., and Cassinelli, J. P. 1986, *Ap. J.*, **310**, 207.
———. 1987, *Ap. J.*, **319**, 850.
Zhou, S., Wu, Y., Evans, N. J., Fuller, G. A., and Myers, P. C. 1989, *Ap. J.*, **346**, 168.

FRED C. ADAMS: MS-51, Harvard-Smithsonian Center for Astrophysics, 60 Garden Street, Cambridge, MA 02138

S. C. CASEY and D. A. HARPER: Yerkes Observatory, Williams Bay, WI 53191

J. A. DAVIDSON: MS 245–6, NASA/Ames Research Center, Moffett Field, CA 94035

G. A. FULLER and P. C. MYERS: MS-42, Harvard-Smithsonian Center for Astrophysics, 60 Garden Street, Cambridge, MA 02138

E. F. LADD: MS-10, Harvard-Smithsonian Center for Astrophysics, 60 Garden Street, Cambridge, MA 02138

R. PADMAN: Cavendish Laboratory, Madingley Road, Cambridge, England CB3 0HE